The Astrophysical Journal, 784:19 (14pp), 2014 March 20 doi:10.1088/0004-637X/784/1/19

HUNTING THE PARENT OF THE ORPHAN STREAM. II. THE FIRST HIGH-RESOLUTION SPECTROSCOPIC STUDY*

Andrew R. Casey[1], Stefan C. Keller[1], Gary Da Costa[1], Anna Frebel[2], and Elizabeth Maunder[1]
[1] Research School of Astronomy and Astrophysics, Australian National University, Canberra, ACT 2611, Australia; andrew.casey@anu.edu.au
[2] Department of Physics, Massachusetts Institute of Technology & Kavli Institute for Astrophysics and Space Research, Cambridge, MA 02139, USA
Received 2013 September 3; accepted 2013 December 17; published 2014 February 27

ABSTRACT

We present the first high-resolution spectroscopic study on the Orphan stream for five stream candidates, observed with the Magellan Inamori Kyocera Echelle spectrograph on the Magellan Clay telescope. The targets were selected from the low-resolution catalog of Casey et al.: three high-probability members, one medium, and one low-probability stream candidate were observed. Our analysis indicates that the low- and medium-probability targets are metal-rich field stars. The remaining three high-probability targets range over ∼1 dex in metallicity, and are chemically distinct compared to the other two targets and all standard stars: low [α/Fe] abundance ratios are observed, and lower limits are ascertained for [Ba/Y], which sit well above the Milky Way trend. These chemical signatures demonstrate that the undiscovered parent system is unequivocally a dwarf spheroidal galaxy, consistent with dynamical constraints inferred from the stream width and arc. As such, we firmly exclude the proposed association between NGC 2419 and the Orphan stream. A wide range in metallicities adds to the similarities between the Orphan stream and Segue 1, although the low [α/Fe] abundance ratios in the Orphan stream are in tension with the high [α/Fe] values observed in Segue 1. Open questions remain before Segue 1 could possibly be claimed as the "parent" of the Orphan stream. The parent system could well remain undiscovered in the southern sky.

Key words: Galaxy: halo – Galaxy: structure – stars: abundances – stars: late-type – stars: Population II

Online-only material: color figures, machine-readable tables

1. INTRODUCTION

A prolonged, quiescent period followed the creation of the Universe. Eventually, minuscule dark matter density perturbations initiated the collapse of dark matter, forming gravitational potential wells and giving rise to the condensation of primordial gas clouds (e.g., Eggen et al. 1962). This process furnished the Universe with the earliest building blocks, laying the foundation for cosmological structure. Separate building blocks (i.e., gas fragments) underwent independent chemical enrichment before conglomerating to form larger systems. Evidence of this hierarchical formation (Searle & Zinn 1978) remains observable today through the accretion of satellite systems onto the Milky Way halo. Although the formation history of the Galaxy is tangled and chaotic, it serves as an excellent—and more importantly, accessible—laboratory to investigate the evolution of the Universe since the earliest times.

Many stars in our Galaxy are formed in situ, but a significant fraction have also been added through the accretion of smaller systems onto the Milky Way (for a review, see Helmi 2008). As these satellite systems move toward the Galaxy's gravitational potential they are disrupted by tidal forces, causing loosely gravitationally bound stars to be strewn in forward and trailing directions as tidal tails or "stellar streams." The observational evidence for ongoing accretion has significantly increased in the last decade since the discovery of the Sagittarius dwarf spheroidal (dSph) undergoing tidal disruption (Ibata et al. 1994; Belokurov et al. 2007; Bell et al. 2008; Starkenburg et al. 2009; Deason et al. 2012; Drake et al. 2013).

Among the known substructures in the halo, the Orphan stream is particularly interesting. Grillmair (2006) and Belokurov et al. (2006) independently discovered the stream, which spans over 60° in the sky from Ursa Major in the north to near Sextans in the south, where the Sloan Digital Sky Survey (SDSS) coverage ends. The stream has properties that are unique from other halo substructures. It has an extremely low surface brightness, ranging from 32 to 40 mag arcsec^{-2}, and a FWHM of ∼2° on sky. At a distance of ∼20 kpc (Belokurov et al. 2007; Grillmair 2006), this corresponds to ∼700 pc. The cross-section and luminosity of the stream are directly related to the mass and velocity dispersion of the parent satellite (Johnston 1998). The Orphan stream width is significantly broader than every known globular cluster tidal tail (Odenkirchen et al. 2003; Grillmair & Johnson 2006; Grillmair & Dionatos 2006a, 2006b) and larger than the tidal diameter of all known globular clusters (Harris 1996, 2010 edition). As Grillmair (2006) notes, if the cross-section of the stream is circular, then in a simple logarithmic potential with $v_c = 220$ km s^{-1}—a reasonable first-order approximation for the Milky Way—the expected random velocities of stars would be required to be $\sqrt{\langle\sigma_v^2\rangle} > 20$ km s^{-1} in order to produce the stream width. Such a velocity dispersion is significantly larger than the expected random motions of stars that have been weakly stripped from a globular cluster, implying that the Orphan stream's progenitor mass must be much larger than a classical globular cluster. Photometry indicates that the stream is metal-poor, implying that negligible star formation has occurred since infall began several billion years ago. For a stream of this length to remain structurally coherent over such a long timescale, the progenitor is also likely to be dark-matter dominated. In their discovery papers, Grillmair (2006) and Belokurov et al. (2007) concluded that the likely parent of the Orphan stream is a low-luminosity dSph galaxy.

Newberg et al. (2010) were able to map the distance and velocity of the stream across the length of the SDSS catalog using blue horizontal branch (BHB) and F-turnoff stars. They found the stream distance to vary between 19 and 47 kpc, extending the 20–32 kpc distance measurements made by

* This paper includes data gathered with the 6.5 m Magellan Telescopes located at Las Campanas Observatory, Chile.

Belokurov et al. (2007), which has been extended to 55 kpc by Sesar et al. (2013). Newberg et al. (2010) note an increase in the density of the Orphan stream near the celestial equator $(l, b) = (253^\circ, 49^\circ)$, proposing that the progenitor may be close to this position. The authors attempted to extend their trace of the stream using southern survey data (e.g., SuperCOSMOS; Hambly et al. 2001), but to no avail; the stream's surface brightness was lower than the survey faint limit. It is still unclear whether the stream extends deep into the southern sky. Newberg et al. (2010) observed an increase in surface brightness near the celestial equator, but given that the stream is closest near the celestial equator (Belokurov et al. 2007), an increase in stream density may be expected given a constant absolute magnitude. Nevertheless, with SDSS photometry and radial velocities from the SEGUE catalog, Newberg et al. (2010) were able to derive a prograde orbit with an eccentricity, apogalacticon, and perigalacticon of $e = 0.7$, 90 kpc, and 16.4 kpc, respectively. The ability to accurately trace the Orphan stream to such extreme distances would make a powerful probe for measuring the galactic potential (e.g., see Price-Whelan & Johnston 2013). From their simulations, Newberg et al. (2010) found a halo and disk mass of $M(R < 60\,\mathrm{kpc}) = 2.6 \times 10^{11}\,M_\odot$, and similarly Sesar et al. (2013) found $2.7 \times 10^{11}\,M_\odot$, which is ∼60% lower than that found by Xue et al. (2008) and Koposov et al. (2007), and slightly lower than the virial mass of $7 \times 10^{11}\,M_\odot$ derived by Sales et al. (2008).

Metallicities derived from SEGUE medium-resolution spectra confirm photometric estimates, indicating that the stream is metal-poor. A mean metallicity of [Fe/H]$= -2.1 \pm 0.1$ dex is found from BHB stars, with a range extending from −1.3 to ∼−3 dex (Newberg et al. 2010). Sesar et al. (2013) also found a wide range in metallicities by tracing RR Lyrae stars along the stream [Fe/H] = −1.5 to −2.7 dex. However, if F-turnoff stars from the Newberg et al. (2010) sample are included, the metallicity distribution function (MDF) extends more metal-rich from ∼−3 to −0.5 dex.

The situation is complicated by interlopers and small number statistics, so the full shape of the MDF is unknown. To this end, Casey et al. (2013a) observed low-resolution spectroscopy for hundreds of stars toward the stream at the celestial equator. The authors targeted the less numerous K-giants (Sales et al. 2008; Morrison 1993, where a mere 1.3 red giant branch stars are expected per square degree) and found a very weak detection of the stream from kinematics alone. Using wide selections in velocity, distance, proper motions, metallicities, and surface gravity, they identified nine highly likely Orphan stream giants. The velocity dispersion of their candidates is within the observational errors ($\sigma_v < 4$ km s^{-1}), suggesting that the stream is kinematically cold along the line of sight. Like Newberg et al. (2010; and independently confirmed by Sesar et al. 2013), they also found an extended range in metallicities: two stars below [Fe/H] $\leqslant -2.70$ and two stars near [Fe/H] ~ -1.17 dex, all of which are consistent with stream membership. The mean metallicity of their sample was [Fe/H]$= -1.63 \pm 0.19$ dex, with a wide dispersion of σ([Fe/H]) = 0.56 dex. It appears that the Orphan stream may have an extremely wide range in metallicity, consistent with the internal chemical enrichment typically observed in dSph galaxies (Mateo 1998; Tolstoy et al. 2009; Kirby et al. 2011; Frebel et al. 2010).

As the name suggests, the Orphan stream's parent satellite has yet to be found. In an effort to identify a progenitor, a number of systems have been identified as being plausibly associated with the Orphan stream. These include the linear Complex A H I clouds, as well as the globular clusters Palomar 1, Arp 2, Terzan 7, and Ruprecht 106. These systems were all identified along the great circle path of the stream. The low-luminosity dwarf satellites Segue 1 and Ursa Major II also lie along the great circle, although Segue 1 was considered an extended globular cluster until recently (Norris et al. 2010; Simon et al. 2011).

Belokurov et al. (2007) first noted a possible association between the Orphan stream, Ursa Major II, and Complex A. Jin & Lynden-Bell (2007) and Fellhauer et al. (2007) explored the possible association between the Orphan stream with Complex A and Ursa Major II, respectively. In the best-fitting Complex A model, the predicted heliocentric velocities did not match those found by Belokurov et al. (2007), or later observations by Newberg et al. (2010). The expected distances were also underestimated by a factor of ∼3 when compared with observations, making the association with Complex A tenuous at best. In the Ursa Major II scenario, the stream's on-sky position was required to exactly overlap with a previous wrap, a somewhat contrived and unlikely scenario. Newberg et al. (2010) found that the Ursa Major II–Orphan stream connection was not compelling either, as the observed stream kinematics were not consistent with the Ursa Major II model.

Simulations involving the Complex A and Ursa Major II associations introduced an a priori assumption that the object (e.g., Ursa Major II or Complex A) was related to the Orphan stream, and consequently found an orbit to match. In contrast, Sales et al. (2008) approached the problem by fitting an orbit to a single wrap of the data, without first assuming a parent satellite. Their *N*-body simulations were inconsistent with either a Complex A or Ursa Major II association. Instead, the authors favored a progenitor with a luminosity $L \sim 2.3 \times 10^4\,L_\odot$ or an absolute magnitude $M_r \sim -6.4$ consistent with the observation by Belokurov et al. (2007) of $M_r \sim -6.7$. Simulations by Sales et al. (2008) suggest the progenitor may be similar to the present-day "classical" Milky Way dwarfs like Carina, Draco, Leo II, or Sculptor, but would be very close to being fully disrupted, which they suggest has occurred over the last 5.3 Gyr. Time of infall is a critical inference. Longer timescales produce streams that are too wide and diffuse, whereas shorter timescales do not reproduce the ∼60° stream length. The degeneracies between these simulation parameters are important to note, but there are robust conclusions that can be drawn irrespective of those degeneracies. For example, Sales et al. (2008) note that a globular cluster has a central density too high ($\sim 10^{12}\,M_\odot\,\mathrm{kpc}^{-3}$) to be fully disrupted along the Orphan stream orbit within a Hubble time. Given this constraint, and the lower limit on luminosity ($L > 2 \times 10^5\,L_\odot$), a globular cluster progenitor seems unlikely from their models.

In addition to the work by Sales et al. (2008), *N*-body simulations by Newberg et al. (2010) exclude all known halo globular clusters as possible progenitors. The authors conclude with the postulation of two possible scenarios: the progenitor is either an undiscovered satellite located between $(l, b) = (250^\circ, 50^\circ)$ and $(270^\circ, 40^\circ)$, or Segue 1 is the parent system. Segue 1, an ultrafaint dwarf galaxy (Simon et al. 2011; Norris et al. 2010), resides at a similar distance (∼23 kpc) along the great circle path of the Orphan stream. Segue 1 also shares velocities that are consistent with the Orphan stream at its nearest point. Moreover, both Segue 1 and the Orphan stream exhibit low velocity dispersions, on the order of ∼4 km s^{-1}. The similarities in position, distance, and velocities between the two systems are indeed striking. However, it

Table 1
Observations

Object[a]	α (J2000)	δ (J2000)	V[b] (mag)	UT Date	UT Time	Airmass	Exp. Time (s)	S/N[c] (pixel^{-1})	V_{hel} (km s^{-1})	V_{err} (km s^{-1})
HD 41667	06:05:03.7	−32:59:36.8	8.52	2011-03-13	23:40:52	1.01	90	272	297.8	1.0
HD 44007	06:18:48.6	−14:50:44.2	8.06	2011-03-13	23:52:18	1.03	30	239	163.4	1.3
HD 76932	08:58:44.2	−16:07:54.2	5.86	2011-03-14	00:16:47	1.16	30	289	119.2	1.2
HD 122563	14:02:31.8	+09:41:09.9	6.02	2011-03-13	07:15:04	1.28	30	230	–23.4	1.0
HD 136316	15:22:17.2	−53:14:13.9	7.65	2011-03-14	09:37:26	1.12	90	335	–38.2	1.1
HD 141531	15:49:16.9	+09:36:42.5	9.08	2011-03-14	09:52:00	1.31	90	280	2.6	1.0
HD 142948	16:00:01.6	−53:51:04.1	8.03	2011-03-14	09:45:12	1.11	90	271	30.3	0.9
OSS 3 (L)	10:46:50.6	−00:13:17.9	17.33	2011-03-14	01:51:07	1.36	4 × 2500	48	217.9	1.0
OSS 6 (H)	10:47:17.8	+00:25:06.9	16.09	2011-03-14	00:25:37	2.00	3 × 1600	59	221.2	1.0
OSS 8 (H)	10:47:30.3	−00:01:22.6	17.25	2011-03-14	04:44:04	1.16	5 × 1900	49	225.9	1.0
OSS 14 (H)	10:49:08.3	+00:01:59.3	16.27	2011-03-15	00:32:17	1.88	4 × 1400	48	225.1	1.0
OSS 18 (M)	10:50:33.7	+00:12:18.3	17.82	2011-03-15	02:12:46	1.30	4 × 2100	31	247.8	1.2

Notes.
[a] Probability of membership (low, medium, high) listed for the Orphan stream candidates as defined by Casey et al. (2013a).
[b] V-band magnitudes for the Orphan stream targets are estimated to be equivalent to g-band magnitudes.
[c] S/N measured per pixel (∼0.09 Å pixel^{-1}) at 600 nm for each target.

is not the only system alleged to be associated with the Orphan stream.

Given the extended apogalacticon of 90 kpc in the stream orbit found by Newberg et al. (2010), Brüns & Kroupa (2011) reasoned that the stream may be the tidal tail of the massive globular cluster NGC 2419. This system is the most distant and luminous outer halo globular cluster known (∼85 kpc, $M_V = -9.6$), and is unlike any other globular cluster in the Milky Way. Spectroscopic studies have confirmed photometric observations by Racine & Harris (1975) that the system is metal-poor ([Fe/H] = −2.15), and identified a remarkable anti-correlation between Mg and K abundances (Cohen et al. 2011; Mucciarelli et al. 2012). The level of magnesium depletion ([Mg/Fe] > −1.40) is not seen anywhere else in the Galaxy or its satellite systems, and neither is the enhanced potassium enrichment (up to [K/Fe] = 2) at the opposite end of this peculiar Mg-K anti-correlation. If NGC 2419 is the parent of the Orphan stream, then this unprecedented chemical signature should exist in disrupted stream members as an example of chemical tagging (e.g., see Freeman & Bland-Hawthorn 2002; De Silva et al. 2007; Wylie-de Boer et al. 2010; Majewski et al. 2012).

In this study, we present an analysis of high-resolution spectroscopic observations for five Orphan stream candidates. The observations and data reduction are outlined in Section 2. In Section 3 we describe the details of our analysis to infer stellar parameters and chemical abundances. We discuss our results in Section 4, including the implications for association between the Orphan stream and the two currently alleged stream progenitors: Segue 1 and NGC 2419. Finally, we conclude in Section 5 with a summary of our findings.

2. OBSERVATIONS AND DATA REDUCTION

High-resolution spectra for five Orphan stream candidates and seven well-studied standard stars have been obtained with the Magellan Inamori Kyocera Echelle spectrograph (Bernstein et al. 2003) on the Magellan Clay telescope. These objects were observed in 2011 March using a 1″ wide slit in mean seeing of 0.″9. This slit configuration provides continuous spectral coverage from 333 nm to 915 nm, with a spectral resolution of $\mathcal{R} = 25{,}000$ in the blue arm and $\mathcal{R} = 28{,}000$ in the red arm. A minimum of 10 exposures of each calibration type (biases, flat fields, and diffuse flats) were observed in the afternoon of each day, with additional flat-field and Th–Ar arc lamp exposures performed throughout the night to ensure an accurate wavelength calibration. The details of our observations are tabulated in Table 1. The signal-to-noise ratio (S/N) ratio for the standard stars exceeds 200 pixel^{-1}, and varies between 30 and 60 for the Orphan stream candidates.

The candidates were chosen from the low-resolution spectroscopic study of Casey et al. (2013a). From their classification, three of the selected stream candidates have a high probability of membership to the Orphan stream. One target was classified with medium probability of membership, and another with a low probability.

Initially we planned to observe many more high-priority targets. However, after our last exposure of target star OSS 18, inclement weather forced us to relinquish the remainder of our observing time. The data were reduced using the CarPy pipeline written by D. Kelson.[3] Every reduced echelle aperture was carefully normalized using cubic splines with defined knot spacing. The extracted apertures were stacked together and weighted by their inverse variance to provide a continuous normalized spectrum for each object.

3. ANALYSIS

Each normalized, stitched spectrum was cross-correlated against a synthetic template to measure the radial velocity of each star. This was performed using a Python[4] implementation of the Tonry & Davis (1979) method. The wavelength region employed was from $845 \leqslant \lambda \leqslant 870$ nm, and a synthetic spectrum of a metal-poor giant was used as the rest template. Heliocentric corrections have been applied to our radial velocity measurements, and the resultant heliocentric velocities are shown in Table 1.

Atomic data for absorption lines was taken from Yong et al. (2005), and these data are listed with their measured equivalent widths (EWs) in Table 2. The EWs for all atomic transitions were measured using the automatic profile fitting algorithm described in Casey et al. (2013b). While this technique is accurate and

[3] http://obs.carnegiescience.edu/Code/mike
[4] http://www.python.org

Table 2
Equivalent Widths for Standard and Program Stars

Wavelength (nm)	Species	χ (eV)	log gf	HD 41667 (mÅ)	HD 44007 (mÅ)	HD 76932 (mÅ)	HD 122563 (mÅ)	HD 136316 (mÅ)	HD 141531 (mÅ)	HD 142948 (mÅ)	OSS 3 (mÅ)
630.030	O I	0.00	−9.72	...	14.8	...	6.8	...	38.2	35.4	...
636.378	O I	0.02	−10.16	11.6	...	...	...	11.6	14.7	12.7	...
568.819	Na I	2.11	−0.42	71.9	30.9	57.4	...	29.3	38.1	...	55.2
615.423	Na I	2.10	−1.53	10.7	...	7.8	...	...	5.2	28.4	...
616.075	Na I	2.10	−1.23	16.6	...	13.4	...	4.6	7.0	43.4	17.4

(This table is available in its entirety in a machine-readable form in the online journal. A portion is shown here for guidance regarding its form and content.)

robust against blended lines as well as strong changes in the local continuum (Frebel et al. 2013; Casey et al. 2013b), every fitted profile was visually inspected for quality. Spurious or false-positive measurements were removed and of the order of ∼5 EW measurements (of the 528 atomic transitions in our line list[5]) were manually re-measured for each object. We excluded transitions with reduced equivalent widths (REW), $\log(\mathrm{EW}/\lambda) > -4.5$, in order to avoid using lines near the flat region of the curve of growth.

Given the range in metallicities for the Orphan stream candidates (see Section 3.1.4), these restrictions resulted in only 14 Fe I and 4 Fe II acceptable transitions for our most metal-poor candidate, OSS 4. With so few lines available, minute changes in stellar parameters caused large trends and variations in the Fe line abundances. This resulted in a poor solution while performing the excitation and ionization equilibria. At this point, we opted to supplement our line list with transitions from Roederer et al. (2010). Each additional transition was inspected in our most metal-rich candidate (OSS 18) to ensure that it was not blended with other features. Blended transitions were not added. As a result, the minimum number of acceptable Fe I and Fe II transitions for any star increased to 48 and 12, respectively.

3.1. Stellar Parameters

We employed the one-dimensional (1D) plane-parallel model atmospheres of Castelli & Kurucz (2004) to infer stellar parameters. These α-enhanced models assume that absorption lines form under local thermal equilibrium, and ignore convective overshoot and any center-to-limb variations. We have interpolated within a grid of these model atmospheres following the prescription in Casey et al. (2013b).

3.1.1. Effective Temperature, T_{eff}

Effective temperatures for all stars have been found by the excitation balance of neutral iron lines. Because all the EW measurements were visually inspected, we generally identified no outlier measurements during this stage. The highest number of Fe I outliers ($>3\sigma$) removed while determining the effective temperature for any star was three. For each iteration in temperature, a linear fit was made to the data (χ, $\log\epsilon(\mathrm{Fe\,I})$). This slope was minimized with successive iterations of effective temperature. Final slopes less than $|10^{-3}|$ dex eV^{-1} were considered to be converged.

The effective temperatures of our standard stars are in excellent agreement with the literature. On average, our effective temperatures are 13 K cooler than the references listed in Table 3. The largest discrepancy exists for HD 122563, a cool metal-poor giant. For extremely metal-poor stars, effective temperatures found through excitation balance are known to produce systematically cooler temperatures than those deduced by other methods (e.g., Frebel et al. 2013). We have chosen to remain consistent with the excitation balance approach, and accept the systematically cooler temperature of 4358 K. The other noteworthy temperature deviant is HD 142948, where we found a temperature 337 K hotter than that found by Gratton et al. (2000). The reason for this discrepancy is not obvious.

3.1.2. Microturbulence, ξ

Microturbulence is necessary in 1D model atmospheres to represent large scale, three-dimensional turbulent motions. The correct microturbulence will ensure that lines of the same species that are formed in deep and shallow photospheric depths will yield the same abundance. We solved for the microturbulence by demanding a zero-trend in REW and abundance for all neutral iron lines. The resultant gradient between REW and abundance is typically $<|0.001|$ dex, and the largest slope in any star is −0.004 dex.

3.1.3. Surface Gravity, log g

The surface gravity for all stars was inferred through the ionization balance of neutral and single ionized Fe lines. We iterated on surface gravity until the mean Fe I abundance matched the mean Fe II abundance to within 0.01 dex. This process was performed in concert while solving for all other stellar parameters. As a consequence of the systematically cooler temperature in HD 122563, we obtained a somewhat lower surface gravity for this star, such that it sits above a metal-poor isochrone on a Hertzsprung–Russell diagram. Modulo HD 122563, the surface gravities for our standard stars are in good agreement with the literature: a mean offset of −0.22 dex is observed (our log g values are lower). This difference remains within the mutual 1σ uncertainties.

3.1.4. Metallicity, $[M/H]$

The final stage of iterative stellar parameter analysis is to derive the total metallicity. For these analyses we adopt the mean [Fe I/H] abundance as the overall metallicity [M/H]. A difference of $|[\mathrm{M/H}] - \langle[\mathrm{Fe\,I/H}]\rangle| \leqslant 0.01$ dex was considered an acceptable model for the data. Excluding HD 122563, the mean metallicity difference for all other standard stars is 0.03 dex less than values in the literature, with a standard deviation of 0.05 dex. When the entire standard sample is included, these values change to −0.07±0.13 dex. Acknowledging that our systematically low temperature for HD 122563 has resulted in differing stellar parameters, we note that the rest of our standard stars exhibit excellent agreement with previous studies. This effect is likely significantly smaller for the metal-poor star OSS

[5] Although our final line list includes atomic data for 528 transitions, we have omitted data for 17 transitions from Table 2 as they were not significantly detected in any stars. See Section 3.3 for details.

Table 3
Stellar Parameters

Object	This Study				Literature				
	$T_{\rm eff}$ (K)	$\log g$ (dex)	ξ (km s^{-1})	[Fe/H] (dex)	$T_{\rm eff}$ (K)	$\log g$ (dex)	ξ (km s^{-1})	[Fe/H] (dex)	Reference
Standard Stars									
HD 41667	4643	1.54	1.81	−1.18	4605	1.88	1.44	−1.16	Gratton et al. (2000)
HD 44007	4820	1.66	1.70	−1.69	4850	2.00	2.20	−1.71	Fulbright (2000)
HD 76932	5835	3.93	1.42	−0.95	5849	4.11	···	−0.88	Nissen et al. (2000)
HD 122563	4358	0.14	2.77	−2.90	4843	1.62	1.80	−2.54	Yong et al. (2013)
HD 136316	4347	0.44	2.15	−1.93	4414	0.94	1.70	−1.90	Gratton & Sneden (1991)
HD 141531	4373	0.52	2.05	−1.65	4280	0.70	1.60	−1.68	Shetrone (1996)
HD 142948	5050	2.39	1.83	−0.64	4713	2.17	1.38	−0.77	Gratton et al. (2000)
Orphan Stream Candidates									
OSS 3 (L)	5225	3.16	1.10	−0.86	···	···	···	−1.31	Casey et al. (2013a)
OSS 6 (H)	4554	0.70	2.00	−1.75	···	···	···	−1.84	Casey et al. (2013a)
OSS 8 (H)	4880	1.71	1.86	−1.62	···	···	···	−1.62	Casey et al. (2013a)
OSS 14 (H)	4675	1.00	2.53	−2.66	···	···	···	−2.70	Casey et al. (2013a)
OSS 18 (M)	5205	2.91	1.88	−0.62	···	···	···	−0.90	Casey et al. (2013a)

14, as this star is further down the giant branch with an effective temperature ∼300 K hotter than HD 122563. Thus, we can be confident in the metallicity determination for OSS 14.

The offsets in metallicities between the values we derive from high-resolution spectroscopy and those found by Casey et al. (2013a) from low-resolution spectroscopy are noticeable. For the high probability targets (OSS 6, 8, and 14) the agreement is excellent: Δ[Fe/H] = +0.04, 0.0, +0.09 dex, respectively. We note that the uncertainties adopted in Casey et al. (2013a) are of the order ±0.3 dex; the discrepancies are well within the 1σ uncertainties of *either* study. The largest difference between this study and that of Casey et al. (2013a) is in the lowest probability target (OSS 3), where we find a metallicity that is +0.45 dex higher.

It is reassuring that the metallicities of our high probability stars show the best agreement with the low-resolution measurements. Candidates were classified by Casey et al. (2013a) to have a low, medium, or high probability of membership with the Orphan stream. This classification was dependent on a number of observables, including metallicity. However, the metallicity determinations by Casey et al. (2013a) were calculated with the implied assumption that these stars were at a distance of ∼20 kpc. The fact that our metallicities from high-resolution spectra are in excellent agreement with these initial metallicities indicates that our initial assumption was correct, and these high probability targets are at the approximate distance to the Orphan stream.[6]

3.2. Uncertainties in Stellar Parameters

During the excitation and ionization equilibria assessments, each fitted slope has an associated uncertainty due to the scatter in iron abundances. We varied the effective temperature and microturbulence to match the formal uncertainty in each Fe I slope. Although these parameters are correlated, we independently varied each parameter to reproduce the slope uncertainty.

In order to estimate the uncertainty in $\log g$, the surface gravity was adjusted until the mean difference in Fe I and Fe II matched the quadrature sum of the variance in Fe I and Fe II abundances. These uncertainties are listed in Table 4 for all standard and program stars. Because these uncertainties were calculated with the assumption that they are uncorrelated, it is possible that they are underestimated. As such we assumed a minimum uncertainty of 125 K in $T_{\rm eff}$, 0.3 dex in $\log g$, and 0.2 km s^{-1} in ξ. Thus, the adopted uncertainty for each star is taken as the maximum of these values and those listed in Table 4.

Table 4
Uncorrelated Uncertainties in Stellar Parameters

Object	$\sigma(T_{\rm eff})$ (K)	$\sigma(\log g)$ (dex)	$\sigma(\xi)$ (km s^{-1})
HD 41667	47	0.08	0.05
HD 44007	51	0.08	0.17
HD 76932	61	0.10	0.14
HD 122563	15	0.01	0.07
HD 136316	34	0.02	0.05
HD 141531	40	0.03	0.05
HD 142948	62	0.12	0.09
OSS 3 (L)	73	0.08	0.11
OSS 6 (H)	39	0.04	0.15
OSS 8 (H)	74	0.17	0.23
OSS 14 (H)	51	0.05	0.13
OSS 18 (M)	135	0.15	0.28

3.3. Chemical Abundances

Chemical abundances are described following the standard nomenclature,[7] and comparisons made with reference to the Sun[8] have been calculated using the solar composition described in Asplund et al. (2009). We note that some transitions were removed from our line list (Table 2) when they were not detected in any star (e.g., Sc I, Zr I, Zr II, Rb I, and Ce II transitions).

3.3.1. Carbon

Carbon was measured by synthesizing the 431.3 nm and 432.3 nm CH features. The best-fitting abundances inferred

[6] We note that to avoid bias from the low-resolution work of Casey et al. (2013a), these high-resolution analyses took place with the information headers removed from each spectrum, and files were re-named to random strings. Original filenames were cross-matched only after the analysis was complete.

[7] $\log\epsilon(X) = \log\left(\frac{N_X}{N_{\rm H}}\right) + 12.$

[8] $\left[\frac{X}{\rm H}\right] = \log\epsilon\left(\frac{N_X}{N_{\rm H}}\right)_{\rm Star} - \log\epsilon\left(\frac{N_X}{N_{\rm H}}\right)_{\rm Sun}.$

from these two syntheses were within 0.05 dex for every star. Nevertheless, we adopted a conservative total uncertainty of ±0.15 dex for these measurements. The mid-point of these two measurements is listed in Table 5. Only the 432.3 nm region was synthesized for OSS 18, as significant absorption of atomic lines was present in the bluer band head, and we deemed the 432.3 nm region to yield a more precise determination of carbon abundance.

3.3.2. Light Odd-Z Elements (Na, Al, K)

Sodium, aluminum, and potassium are primarily produced through carbon, neon, and oxygen burning in massive stars before they are ejected into the interstellar medium (Woosley & Weaver 1995).

Although our line list includes three clean, unblended Na lines, not all were detectable in the Orphan stream candidates. Generally, only one Na and Al line was available for the Orphan stream stars. In these cases, a minimum standard deviation of 0.10 dex was assumed when calculating abundance uncertainties (see Section 3.4). Wherever there were no detectable lines for a given element, an upper limit was determined by synthesis of the strongest transition in our line list. At least one K line was detected in every standard and program star. These lines at 766 nm and 769 nm are quite strong, but fall directly between a strong telluric band head. Usually both lines were detected, but one was dominated by the Earth's atmospheric absorption. In these cases, we rejected the contaminated line and adopted the single, unaffected K line.

3.3.3. α-elements (O, Mg, Ca, Si, Ti)

The α-elements (O, Mg, Ca, Si, and Ti) are produced during hydrostatic burning of carbon, neon, and silicon by α-particle capture. Following Type II supernovae, the α-enriched material is dispersed into the interstellar medium and contributes to the next generation of star formation. Although Ti is not formally an α-element ($Z = 22$), it generally tracks with α-elements, and has been included here to facilitate a comparison with the Local Group study of Venn et al. (2004).

Generally, the Orphan stream candidates have lower α-element abundances compared to iron than their halo counterparts. The situation is a little ambiguous for [O/Fe] compared to other α-elements. We employed the forbidden lines at 630 nm and 636 nm to measure oxygen abundances in our stars. Given the weakness of these lines, oxygen was immeasurable in all of the Orphan stream candidates. In place of abundances, upper limits were determined from spectral synthesis of the region. The synthesis line list includes the Ni I feature hidden within the 630 nm absorption profile (Allende Prieto et al. 2001). In the low S/N ratio case of OSS 18, the forbidden oxygen region was sufficiently dominated by telluric absorption, such that we deemed even a robust upper limit to be indeterminable.

The [Mg/Fe] abundance ratios for the Orphan stream targets are noticeably lower than any of the other α-elements. In fact, OSS 18 and 3 exhibit solar or sub-solar [Mg/Fe] abundances, and the mean [α/Fe] abundances in the lower panel of Figure 1 are most affected by [Mg/Fe]. Nevertheless, the [Ca/Fe] and [Si/Fe] abundances for the Orphan stream targets are systematically lower than their Milky Way counterparts. In Figure 1, Ti II has been adopted for [Ti/Fe], as few reliable Ti I transitions were available for analysis.

Lower [α/Fe] abundance ratios are less apparent for our lower probability Orphan stream candidates, OSS 18 and OSS 3. Although their mean [α/Fe] ∼ +0.20 dex, with [Fe/H] ∼ −0.70 dex they are significantly more metal-rich than expected for the Orphan stream. Therefore, their [α/Fe] abundance ratios are consistent with the [α/Fe]–[Fe/H] trend of the Milky Way. As discussed further in Section 4.1, these low probability targets are unlikely to be true Orphan stream members, and are marked appropriately in Figure 1.

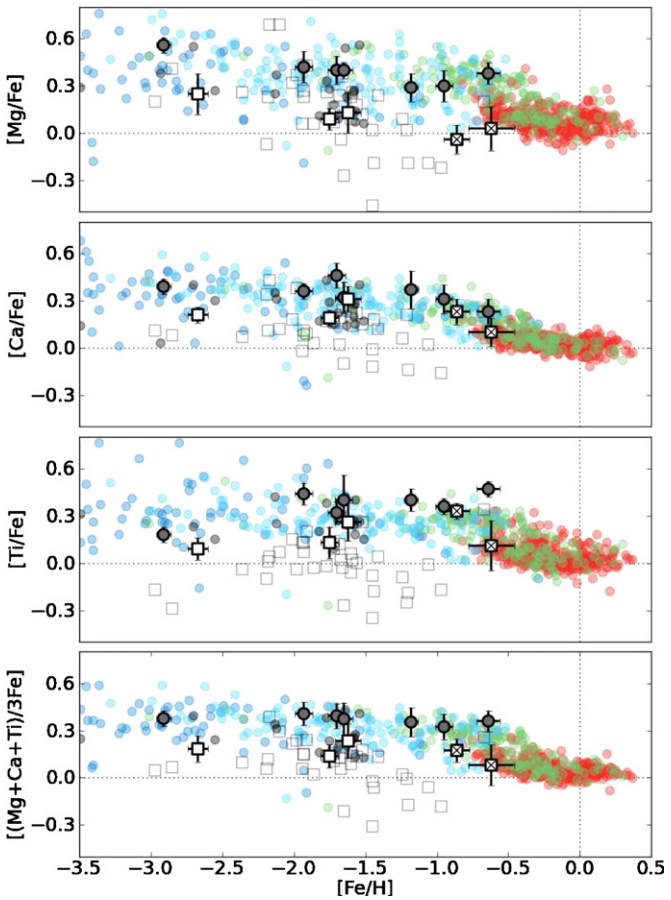

Figure 1. α-element abundance ratios (Mg I, Ca I, Ti II shown) for field standards (gray, filled), high-probability Orphan stream candidates (white squares), and lower-probability Orphan stream candidates (white squares with crosses) that are deemed to be interlopers. Data compiled by Venn et al. (2004, 2006) for the present-day dSph galaxies (gray squares) and the Milky Way are shown, using the same color scheme adopted in Venn et al. (2004): thin disk (red), thick disk (green), halo (cyan), high velocity halo (dark blue), and retrograde halo stars (black).

(A color version of this figure is available in the online journal.)

3.3.4. Fe-peak Elements (Sc, V, Cr, Mn, Co, Ni, Cu, Zn)

The Fe-peak elements ($Z = 23$–30) are primarily produced by explosive nucleosynthesis during oxygen, neon, and silicon burning. The ignition of these burning phases occurs from Type II SN of massive stars, as well as when an accreting white dwarf exceeds the Chandrasekhar limit, which causes spontaneous ignition of carbon and an eventual Type Ia supernova. The abundance of the Fe-peak elements with respect to iron in the Milky Way is typically either flat (i.e., [X/Fe] ∼ 0; Cr II, Ni) or trend positively (Sc, Cr I, Mn, Cu) with overall [Fe/H] (e.g., Ishigaki et al. 2013; Yong et al. 2013).

Scandium absorption profiles have appreciable broadening due to hyperfine splitting. As such, we determined Sc abundances for all stars from spectral synthesis with hyperfine splitting taken into account. However, for OSS 3 we found the broadening due to hyperfine structure to be negligible, and

Table 5
Chemical Abundances

Species	N	$\log\epsilon(X)$	σ	$[X/H]$	$[X/Fe]$	$\sigma_{\bar{x}}$	Species	N	$\log\epsilon(X)$	σ	$[X/H]$	$[X/Fe]$	$\sigma_{\bar{x}}$
			HD 41667							HD 44007			
C (CH)	2	6.95	0.20	−1.48	−0.24	0.15	C (CH)	2	6.73	0.20	−1.70	−0.01	0.15
O I	1	7.85	···	−0.84	0.34	···	O I	1	7.43	···	−1.26	0.44	···
Na I	3	4.95	0.10	−1.29	−0.10	0.06	Na I	1	4.57	···	−1.67	0.03	···
Mg I	7	6.71	0.13	−0.89	0.29	0.05	Mg I	5	6.29	0.06	−1.31	0.40	0.03
Al I	4	5.27	0.11	−1.18	−0.00	0.05	Al I	0	···	···	···	···	···
Si I	8	6.58	0.14	−0.93	0.26	0.05	Si I	7	6.18	0.09	−1.33	0.37	0.03
K I	2	4.66	0.00	−0.38	0.81	0.00	K I	2	4.43	0.05	−0.60	1.10	0.04
Ca I	18	5.52	0.07	−0.82	0.37	0.02	Ca I	20	5.10	0.09	−1.24	0.46	0.02
Sc II	14	2.10	0.10	−1.05	0.13	0.03	Sc II	12	1.45	0.08	−1.70	0.00	0.02
Ti I	25	3.90	0.16	−1.05	0.13	0.03	Ti I	20	3.35	0.08	−1.60	0.11	0.02
Ti II	28	4.16	0.18	−0.79	0.40	0.03	Ti II	36	3.57	0.13	−1.38	0.32	0.02
V I	4	2.82	0.09	−1.11	0.07	0.05	V I	4	2.24	0.05	−1.69	0.01	0.02
Cr I	12	4.28	0.07	−1.36	−0.18	0.02	Cr I	15	3.75	0.06	−1.89	−0.19	0.02
Cr II	3	4.65	0.13	−0.99	0.20	0.08	Cr II	3	4.10	0.04	−1.54	0.16	0.03
Mn I	5	4.12	0.17	−1.31	−0.13	0.08	Mn I	7	3.30	0.10	−2.13	−0.43	0.04
Fe I	72	6.32	0.11	−1.18	0.00	0.01	Fe I	74	5.80	0.12	−1.70	0.00	0.01
Fe II	17	6.32	0.08	−1.18	0.00	0.02	Fe II	17	5.80	0.12	−1.70	0.01	0.03
Co I	4	3.85	0.05	−1.14	0.04	0.03	Co I	3	3.29	0.09	−1.70	0.00	0.05
Ni I	20	4.96	0.13	−1.26	−0.08	0.03	Ni I	23	4.46	0.12	−1.76	−0.05	0.03
Cu I	1	2.86	···	−1.33	−0.15	···	Cu I	1	1.90	···	−2.29	−0.59	···
Zn I	2	3.39	0.04	−1.17	0.01	0.03	Zn I	2	2.88	0.08	−1.68	0.02	0.06
Sr II	1	1.75	···	−1.12	0.06	···	Sr II	1	1.19	···	−1.68	0.02	···
Y II	3	1.08	0.12	−1.13	0.05	0.07	Y II	3	0.35	0.06	−1.86	−0.15	0.04
Ba II	2	0.97	0.03	−1.21	−0.02	0.02	Ba II	2	0.43	0.08	−1.75	−0.04	0.05
La II	2	0.14	0.03	−0.97	0.22	0.02	La II	2	−0.42	0.00	−1.52	0.18	0.00
Nd II	6	0.56	0.06	−0.86	0.32	0.02	Nd II	7	−0.26	0.09	−1.68	0.03	0.03
Eu II	1	−0.16	···	−0.68	0.50	···	Eu II	1	−1.16	···	−1.68	0.02	···
			HD 76932							HD 122563			
C (CH)	2	7.63	0.20	−0.79	0.15	0.15	C (CH)	2	5.26	0.20	−3.17	−0.27	0.15
O I	1	<8.33	···	<−0.36	<0.58	···	O I	1	6.15	···	−2.54	0.37	···
Na I	3	5.44	0.03	−0.80	0.15	0.02	Na I	1	<3.48	···	<−2.76	<0.14	···
Mg I	8	6.94	0.18	−0.66	0.30	0.06	Mg I	8	5.25	0.08	−2.35	0.56	0.03
Al I	4	5.56	0.08	−0.89	0.07	0.04	Al I	1	<4.83	···	<−1.62	<1.28	···
Si I	9	6.80	0.18	−0.71	0.24	0.06	Si I	1	5.21	···	−2.30	0.61	···
K I	2	4.96	0.06	−0.07	0.89	0.05	K I	1	2.75	···	−2.28	0.63	···
Ca I	23	5.69	0.09	−0.65	0.31	0.02	Ca I	19	3.81	0.05	−2.53	0.39	0.01
Sc II	16	2.38	0.10	−0.77	0.18	0.02	Sc II	15	0.17	0.07	−2.98	−0.07	0.02
Ti I	17	4.16	0.06	−0.79	0.16	0.01	Ti I	17	2.06	0.04	−2.89	0.02	0.01
Ti II	38	4.35	0.12	−0.60	0.36	0.02	Ti II	42	2.22	0.10	−2.73	0.18	0.02
V I	4	3.28	0.12	−0.65	0.31	0.06	V I	1	0.81	···	−3.12	−0.21	···
Cr I	18	4.58	0.07	−1.06	−0.11	0.02	Cr I	11	2.39	0.08	−3.25	−0.34	0.02
Cr II	3	4.86	0.04	−0.78	0.18	0.02	Cr II	3	2.83	0.03	−2.81	0.10	0.02
Mn I	9	4.31	0.10	−1.12	−0.17	0.03	Mn I	7	2.12	0.06	−3.31	−0.39	0.02
Fe I	96	6.55	0.11	−0.95	0.00	0.01	Fe I	165	4.59	0.11	−2.91	0.00	0.01
Fe II	20	6.55	0.13	−0.95	0.00	0.03	Fe II	22	4.60	0.11	−2.90	0.01	0.02
Co I	4	4.09	0.12	−0.90	0.05	0.06	Co I	5	2.23	0.14	−2.76	0.15	0.06
Ni I	25	5.32	0.11	−0.90	0.05	0.02	Ni I	19	3.48	0.10	−2.74	0.17	0.02
Cu I	1	2.95	···	−1.24	−0.29	···	Cu I	1	<0.10	···	<−4.19	<−1.19	···
Zn I	2	3.71	0.02	−0.85	0.10	0.01	Zn I	2	1.83	0.06	−2.72	0.19	0.05
Sr II	1	2.00	···	−0.87	0.08	···	Sr II	1	−0.64	···	−3.51	−0.60	···
Y II	2	1.29	0.04	−0.92	0.03	0.02	Y II	1	−0.82	···	−3.03	−0.12	···
Ba II	2	1.34	0.04	−0.84	0.12	0.03	Ba II	2	−1.94	0.06	−4.12	−1.20	0.04
La II	1	0.69	···	−0.41	0.54	···	La II	1	<−1.51	···	<−2.61	<0.29	···
Nd II	3	0.81	0.11	−0.61	0.35	0.07	Nd II	1	<−1.83	···	<−3.25	<−0.35	···
Eu II	1	<−0.27	···	<−0.79	<0.15	···	Eu II	1	<−1.72	···	<−2.24	<0.66	···
			HD 136316							HD 141531			
C (CH)	2	6.05	0.20	−2.38	−0.47	0.15	C (CH)	2	6.31	0.20	−2.12	−0.42	0.15
O I	1	7.11	···	−1.58	0.35	···	O I	2	7.36	0.01	−1.33	0.31	0.00
Na I	2	4.21	0.08	−2.03	−0.10	0.06	Na I	3	4.40	0.07	−1.84	−0.19	0.04
Mg I	8	6.09	0.29	−1.51	0.42	0.10	Mg I	9	6.36	0.27	−1.24	0.40	0.09
Al I	1	<4.58	···	<−1.87	<0.04	···	Al I	1	4.82	···	−1.63	0.01	···
Si I	8	5.93	0.17	−1.58	0.35	0.06	Si I	7	6.08	0.15	−1.43	0.21	0.06
K I	2	3.83	0.03	−1.21	0.72	0.02	K I	2	4.13	0.06	−0.90	0.74	0.04

Table 5
(Continued)

Species	N	$\log\epsilon(X)$	σ	[X/H]	[X/Fe]	$\sigma_{\bar{x}}$	Species	N	$\log\epsilon(X)$	σ	[X/H]	[X/Fe]	$\sigma_{\bar{x}}$
Ca I	19	4.77	0.08	−1.57	0.36	0.02	Ca I	17	5.02	0.06	−1.32	0.32	0.01
Sc II	16	1.24	0.08	−1.91	0.01	0.02	Sc II	12	1.56	0.05	−1.59	0.05	0.01
Ti I	26	3.02	0.13	−1.93	−0.01	0.03	Ti I	26	3.34	0.13	−1.61	0.03	0.03
Ti II	39	3.46	0.18	−1.49	0.44	0.03	Ti II	32	3.70	0.17	−1.25	0.40	0.03
V I	6	1.88	0.08	−2.05	−0.12	0.03	V I	6	2.24	0.10	−1.69	−0.05	0.04
Cr I	18	3.52	0.13	−2.12	−0.20	0.03	Cr I	15	3.78	0.07	−1.86	−0.22	0.02
Cr II	2	3.83	0.03	−1.81	0.11	0.02	Cr II	1	4.14	···	−1.50	0.14	···
Mn I	9	3.14	0.14	−2.29	−0.36	0.05	Mn I	7	3.44	0.15	−1.99	−0.35	0.06
Fe I	100	5.57	0.12	−1.93	0.00	0.01	Fe I	83	5.85	0.12	−1.65	0.00	0.01
Fe II	16	5.57	0.08	−1.93	0.00	0.02	Fe II	17	5.85	0.08	−1.65	0.00	0.02
Co I	4	3.08	0.12	−1.91	0.01	0.06	Co I	6	3.33	0.13	−1.66	−0.01	0.05
Ni I	24	4.24	0.12	−1.98	−0.05	0.03	Ni I	25	4.50	0.15	−1.72	−0.07	0.03
Cu I	1	1.72	···	−2.47	−0.54	···	Cu I	1	2.15	···	−2.04	−0.40	···
Zn I	2	2.65	0.10	−1.91	0.02	0.07	Zn I	2	2.79	0.04	−1.77	−0.13	0.03
Sr II	1	0.90	···	−1.97	−0.04	···	Sr II	1	1.20	···	−1.67	−0.03	···
Y II	3	0.12	0.10	−2.09	−0.16	0.06	Y II	3	0.35	0.10	−1.86	−0.21	0.06
Ba II	2	0.19	0.08	−1.99	−0.06	0.06	Ba II	2	0.47	0.05	−1.71	−0.07	0.04
La II	2	−0.73	0.03	−1.83	0.09	0.02	La II	2	−0.54	0.07	−1.65	0.00	0.05
Nd II	8	−0.40	0.04	−1.82	0.10	0.02	Nd II	7	−0.18	0.07	−1.60	0.04	0.03
Eu II	1	−1.12	···	−1.64	0.29	···	Eu II	1	−0.93	···	−1.45	0.19	···
		HD 142948							OSS 3				
C (CH)	2	7.75	0.15	−0.68	0.03	0.15	C (CH)	2	7.54	0.15	−0.89	0.00	0.15
O I	2	8.57	0.02	−0.12	0.52	0.01	O I	1	<8.41	···	<−0.27	<0.52	···
Na I	2	5.69	0.02	−0.55	0.09	0.01	Na I	2	5.22	0.01	−1.02	−0.16	0.01
Mg I	6	7.34	0.10	−0.26	0.38	0.04	Mg I	6	6.70	0.14	−0.90	−0.04	0.06
Al I	4	6.03	0.09	−0.42	0.22	0.04	Al I	2	5.27	0.11	−1.18	−0.32	0.08
Si I	8	7.10	0.15	−0.41	0.23	0.05	Si I	8	6.72	0.16	−0.79	0.07	0.06
K I	1	5.17	0.00	0.14	0.78	0.00	K I	1	4.85	···	−0.18	0.68	···
Ca I	18	5.93	0.11	−0.41	0.23	0.03	Ca I	21	5.71	0.13	−0.63	0.23	0.03
Sc II	13	2.81	0.09	−0.34	0.30	0.03	Sc II	11	2.24	0.09	−0.91	−0.05	0.03
Ti I	22	4.44	0.10	−0.51	0.14	0.02	Ti I	19	4.17	0.15	−0.78	0.08	0.03
Ti II	31	4.77	0.20	−0.18	0.47	0.04	Ti II	37	4.42	0.24	−0.53	0.33	0.04
V I	4	3.44	0.09	−0.49	0.15	0.05	V I	2	2.97	0.05	−0.88	−0.02	0.04
Cr I	11	4.82	0.05	−0.82	−0.17	0.01	Cr I	17	4.73	0.20	−0.91	−0.05	0.05
Cr II	2	5.11	0.01	−0.53	0.11	0.00	Cr II	3	4.89	0.26	−0.75	0.11	0.15
Mn I	8	4.74	0.18	−0.69	−0.05	0.06	Mn I	3	4.05	0.03	−1.38	−0.42	0.02
Fe I	68	6.86	0.13	−0.64	0.00	0.02	Fe I	97	6.64	0.20	−0.86	0.00	0.02
Fe II	16	6.87	0.14	−0.63	0.01	0.03	Fe II	27	6.64	0.24	−0.86	0.00	0.05
Co I	5	4.49	0.08	−0.50	0.14	0.04	Co I	4	4.27	0.26	−0.72	0.14	0.13
Ni I	21	5.62	0.16	−0.60	0.04	0.03	Ni I	25	5.33	0.24	−0.89	−0.03	0.05
Cu I	1	3.90	···	−0.29	0.35	···	Cu I	1	2.53	···	−1.66	−0.80	···
Zn I	2	4.13	0.00	−0.42	0.22	0.00	Zn I	2	3.67	0.15	−0.89	−0.03	0.10
Sr II	1	2.40	···	−0.47	0.17	···	Sr II	1	1.95	···	−0.92	−0.06	···
Y II	3	1.74	0.24	−0.47	0.17	0.14	Y II	2	1.28	0.35	−0.93	−0.07	0.25
Ba II	2	1.44	0.02	−0.74	−0.09	0.01	Ba II	2	1.52	0.13	−0.66	0.20	0.09
La II	2	0.61	0.10	−0.49	0.15	0.07	La II	1	<0.57	···	<−1.53	<0.36	···
Nd II	4	1.02	0.07	−0.40	0.24	0.04	Nd II	1	1.46	···	0.04	0.90	···
Eu II	1	0.25	···	−0.27	0.37	···	Eu II	1	<−0.09	···	<−0.61	<0.28	···
		OSS 6							OSS 8				
C (CH)	2	6.39	0.20	−2.04	−0.37	0.15	C (CH)	2	6.85	0.20	−1.58	0.00	0.15
O I	1	<7.08	···	<−1.61	<0.06	···	O I	1	<7.46	···	<−1.23	<0.35	···
Na I	1	4.26	···	−1.98	−0.23	···	Na I	1	4.36	···	−1.88	−0.26	···
Mg I	6	5.94	0.21	−1.66	0.09	0.09	Mg I	6	6.10	0.15	−1.49	0.13	0.06
Al I	1	4.84	···	−1.61	0.14	···	Al I	1	<5.21	···	<−1.24	<0.34	···
Si I	3	5.84	0.07	−1.67	0.09	0.04	Si I	2	6.01	0.13	−1.50	0.12	0.09
K I	1	3.86	···	−1.17	0.58	···	K I	1	4.24	···	−0.79	0.83	···
Ca I	21	4.78	0.15	−1.56	0.19	0.03	Ca I	22	5.03	0.14	−1.31	0.31	0.03
Sc II	5	1.10	0.10	−2.05	−0.31	0.05	Sc II	16	1.47	0.15	−1.68	−0.06	0.04
Ti I	23	3.09	0.18	−1.86	−0.11	0.04	Ti I	20	3.31	0.11	−1.64	−0.02	0.02
Ti II	35	3.33	0.19	−1.62	0.13	0.03	Ti II	37	3.59	0.21	−1.36	0.26	0.03
V I	2	1.74	0.12	−2.19	−0.44	0.08	V I	2	2.29	0.18	−1.64	−0.02	0.13
Cr I	20	3.71	0.13	−1.93	−0.18	0.03	Cr I	17	3.82	0.12	−1.82	−0.19	0.03
Cr II	2	4.10	0.06	−1.54	0.21	0.04	Cr II	3	4.23	0.04	−1.41	0.21	0.02
Mn I	2	3.23	0.01	−2.20	−0.45	0.01	Mn I	5	3.53	0.18	−1.90	−0.28	0.08

Table 5
(Continued)

Species	N	$\log\epsilon(X)$	σ	[X/H]	[X/Fe]	$\sigma_{\bar{x}}$	Species	N	$\log\epsilon(X)$	σ	[X/H]	[X/Fe]	$\sigma_{\bar{x}}$
Fe I	66	5.75	0.11	−1.75	0.00	0.01	Fe I	60	5.88	0.15	−1.62	0.00	0.02
Fe II	15	5.74	0.13	−1.76	0.00	0.03	Fe II	12	5.88	0.16	−1.62	0.00	0.05
Co I	3	3.00	0.36	−1.99	−0.23	0.21	Co I	4	3.35	0.14	−1.64	−0.02	0.07
Ni I	22	4.39	0.13	−1.83	−0.08	0.03	Ni I	20	4.52	0.15	−1.70	−0.08	0.03
Cu I	1	1.02	···	−3.17	−1.42	···	Cu I	1	1.68	···	−2.51	−0.89	···
Zn I	2	2.46	0.14	−2.09	−0.34	0.10	Zn I	1	2.89	···	−1.67	−0.05	···
Sr II	1	0.73	···	−2.14	−0.39	···	Sr II	1	0.79	···	−2.08	−0.46	···
Y II	1	<−0.59	···	<−2.77	<−1.10	···	Y II	1	<−0.41	···	<−2.60	<−1.00	···
Ba II	1	−0.08	···	−2.26	−0.50	···	Ba II	2	0.04	0.20	−2.14	−0.51	0.14
La II	1	<−1.00	···	<−1.82	<−0.35	···	La II	1	−0.12	···	−1.22	0.40	···
Nd II	2	−0.71	0.08	−2.13	−0.38	0.06	Nd II	1	0.08	···	−1.34	0.28	···
Eu II	1	<−1.45	···	<−1.97	<−0.30	···	Eu II	1	<−0.62	···	<−1.14	<0.44	···
		OSS 14							OSS 18				
C (CH)	2	5.85	0.20	−2.58	0.08	0.15	C (CH)	1	7.57	0.20	−0.86	−0.10	0.15
O I	1	<6.40	···	<−2.09	<0.57	···	O I	0	···	···	···	···	···
Na I	1	<3.87	···	<−2.37	<0.29	···	Na I	1	5.37	···	−0.87	−0.25	···
Mg I	8	5.19	0.21	−2.41	0.25	0.07	Mg I	5	7.01	0.25	−0.59	0.03	0.11
Al I	0	···	···	···	···	···	Al I	1	<5.66	···	<−0.79	<−0.03	···
Si I	2	5.50	0.04	−2.00	0.66	0.02	Si I	5	6.98	0.28	−0.53	0.09	0.13
K I	1	2.66	···	−2.37	0.30	···	K I	1	4.91	···	−0.12	0.50	···
Ca I	16	3.89	0.15	−2.45	0.21	0.04	Ca I	19	5.82	0.14	−0.52	0.10	0.03
Sc II	9	0.13	0.13	−3.02	−0.35	0.04	Sc II	11	2.64	0.18	−0.51	0.11	0.05
Ti I	11	2.24	0.12	−2.71	−0.05	0.04	Ti I	17	4.27	0.24	−0.68	−0.06	0.06
Ti II	32	2.37	0.18	−2.58	0.09	0.03	Ti II	25	4.44	0.33	−0.51	0.11	0.07
V I	1	<1.61	···	<−2.32	<0.34	···	V I	4	3.26	0.01	−0.67	−0.05	0.00
Cr I	10	2.54	0.23	−3.10	−0.43	0.07	Cr I	18	4.83	0.28	−0.81	−0.19	0.06
Cr II	1	3.06	···	−2.58	0.09	···	Cr II	1	5.29	···	−0.35	0.27	···
Mn I	4	2.20	0.20	−3.23	−0.56	0.10	Mn I	3	4.30	0.09	−1.13	−0.51	0.05
Fe I	133	4.83	0.20	−2.67	0.00	0.02	Fe I	48	6.88	0.21	−0.62	0.00	0.03
Fe II	16	4.83	0.16	−2.67	−0.01	0.04	Fe II	12	6.88	0.25	−0.62	0.00	0.07
Co I	3	2.32	0.48	−2.67	−0.01	0.28	Co I	3	4.65	0.41	−0.34	0.28	0.24
Ni I	5	3.51	0.07	−2.71	−0.04	0.03	Ni I	17	5.43	0.24	−0.79	−0.17	0.06
Cu I	1	<0.77	···	<−3.42	<−0.75	···	Cu I	1	3.14	···	−1.05	−0.43	···
Zn I	1	<1.92	···	<−2.64	<0.02	···	Zn I	1	3.87	···	−0.69	−0.07	···
Sr II	1	−0.22	···	−3.09	−0.42	···	Sr II	1	2.31	···	−0.56	0.06	···
Y II	1	<−0.86	···	<−3.10	<−0.40	···	Y II	1	1.92	···	−0.29	0.33	···
Ba II	2	−1.85	0.05	−4.04	−1.37	0.04	Ba II	2	1.76	0.05	−0.42	0.20	0.04
La II	1	<−0.91	···	<−2.01	<0.65	···	La II	1	1.29	···	0.19	0.81	···
Nd II	1	<−0.56	···	<−1.98	<0.68	···	Nd II	2	1.71	0.02	0.29	0.91	0.01
Eu II	1	<−1.14	···	<−1.66	<1.00	···	Eu II	1	0.72	···	0.20	0.82	···

the variance in our synthesis measurements was larger than our abundance measurements. The mean Sc II abundance to be $\log\epsilon(\mathrm{Sc}) = 2.22 \pm 0.23$ from synthesis of five lines, where the EWs of 11 Sc II lines yields $\log\epsilon(\mathrm{Sc}) = 2.24 \pm 0.09$. Therefore, in the case of OSS 3, we adopted the Sc II abundances from the EWs.

Other Fe-peak elements with hyperfine structures (e.g., V, Mn, Co, and Cu) have been synthesized with the relevant isotopic and/or hyperfine splitting included. The random measurement scatter in V, Cr, and Mn abundances is typically low (<0.05 dex) for all the standard and program stars. However, for Co, there was a noticeable increase in the line-to-line scatter for the Orphan stream stars compared to the standard stars. There is a factor of ∼6 difference in S/N ratio between the two samples that can explain this variance. In the Orphan stream stars, no synthesized Co profiles were sufficiently "worse" than each other to qualify exclusion. The case was quite different for Ni, where a plethora of clean lines (without an appreciable hyperfine structure) are available, and the uncertainties in $\log\epsilon$(Ni) abundances due to the uncertainties in stellar parameters generally cancel with $\log\epsilon$(Fe), yielding excellent measurements of [Ni/Fe]. Cu abundances and upper limits are derived from the synthesis of a single neutral Cu line at 510.5 nm. The inclusion of a hyperfine structure was most important for Cu, as a Cu abundance measured directly from an EW produced a systematically higher $\log\epsilon$(Cu), on the order of +0.4 dex. Zn abundances were calculated directly from the EWs of the 472.2 nm and 481.0 nm transitions, where available. All of our Fe-peak abundances with respect to iron are consistent with the observed chemical trends in the Milky Way (Ishigaki et al. 2013; Yong et al. 2013).

3.3.5. Neutron-capture Elements (Sr, Y, Ba, La, Nd, Eu)

The atomic absorption lines of these heavy elements have appreciable broadening due to hyperfine structure and isotopic splitting. Where applicable, the relevant hyperfine and/or isotopic splitting was employed, and solar isotopic compositions were adopted.

Sr and Y are elements of the first *n*-capture peak. While only one line (421.5 nm) was synthesized for Sr II, three unblended Y lines were available. When no Y lines were detected above 3σ, an upper limit was ascertained from the 520 nm line—the

Table 6
Abundance Uncertainties Due to Stellar Parameters

Species	$T_{\rm eff}+\sigma(T_{\rm eff})$ Δabundance	$\log g+\sigma(\log g)$ Δabundance	$v_t+\sigma(v_t)$ Δabundance	Max(0.10, S.D.)/$\sqrt{(N)}$ (dex)	Total Uncertainty [X/H] (dex)	Total Uncertainty [X/Fe] (dex)
			OSS 3			
Na I	+0.06	+0.00	−0.01	0.07	0.09	0.08
Mg I	+0.07	−0.02	−0.02	0.06	0.09	0.18
Al I	+0.04	+0.00	+0.00	0.08	0.09	0.10
Si I	+0.03	+0.01	−0.01	0.06	0.07	0.08
K I	+0.07	−0.03	−0.04	0.10	0.13	0.23
Ca I	+0.07	−0.02	−0.03	0.03	0.08	0.17
Sc II	+0.00	+0.03	−0.03	0.03	0.05	0.19
Ti I	+0.12	−0.01	−0.05	0.03	0.14	0.14
Ti II	+0.01	+0.02	−0.06	0.04	0.07	0.15
V I	+0.12	+0.00	−0.03	0.06	0.13	0.06
Cr I	+0.11	−0.01	−0.06	0.05	0.13	0.13
Cr II	−0.02	+0.04	−0.04	0.15	0.16	0.15
Mn I	+0.10	−0.02	−0.03	0.11	0.16	0.21
Fe I	+0.08	+0.00	−0.04	0.02	0.09	...
Fe II	−0.03	+0.04	−0.03	0.05	0.07	...
Co I	+0.11	−0.01	−0.07	0.13	0.19	0.19
Ni I	+0.07	+0.00	−0.04	0.05	0.09	0.04
Cu I	+0.10	+0.01	−0.05	0.10	0.15	0.06
Zn I	+0.00	+0.02	−0.04	0.10	0.11	0.11
Sr II	+0.03	+0.00	−0.01	0.10	0.10	0.11
Y II	+0.01	+0.03	−0.02	0.25	0.25	0.16
Ba II	+0.02	+0.01	−0.06	0.09	0.11	0.05
Nd II	+0.04	+0.04	−0.04	0.10	0.12	0.21

(This table is available in its entirety in a machine-readable form in the online journal. A portion is shown here for guidance regarding its form and content.)

strongest in our line list. Sr and Y abundances generally agreed with each other in our stars, with the exception of the high probability stream candidates, OSS 6 and OSS 8. In these cases only upper limits could be determined for Y II, and those limits were ∼0.6 dex lower than our measured Sr II abundances. The remaining high probability candidate, OSS 14, also has an upper limit for Y II ([Y/Fe] < -0.40) but this limit is much closer to our Sr II measurement ([Sr/Fe] $= -0.42$). The Y upper limits for our high probability Orphan stream stars results in lower limits for [Ba/Y], which, for OSS 6 and OSS 8, are well in excess of the Milky Way trend (Figure 2).

Lanthanum and neodymium abundances for our stars are consistent with the chemical evolution of the Milky Way. Europium, a *r*-process dominated element, was measured by synthesizing the 664.5 nm Eu II transition. Although the spread in [Eu/Fe] abundances for our stars is wide, no significant *r*-process enhancement was observed.

3.4. Chemical Abundance Uncertainties Due to Stellar Parameters

Although the standard error about the mean ($\sigma_{\bar{x}}$) abundance in Table 5 can be quite low, the uncertainties in stellar parameters will significantly contribute to the total error budget for any given abundance. Furthermore, the total uncertainty in abundance ratios (e.g., [A/B]) depends on how the uncertainties in elements A and B are correlated with stellar parameters.

In order to investigate the abundance uncertainties due to stellar parameters, we generated model atmospheres for a $\pm1\sigma$ offset in each stellar parameter (Section 3.2; $T_{\rm eff}$, $\log g$, ξ) independently, and calculated the resultant mean abundance offset from our EWs. The resultant abundance changes were

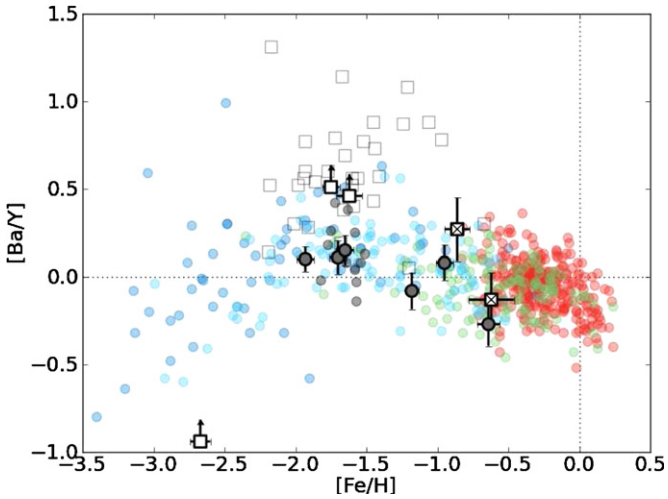

Figure 2. [Ba/Y] abundance ratios for the Orphan stream stars and field standards. Milky Way and dSph data compiled by Venn et al. (2004) is also shown. Markers and colors are the same as described in Figure 1.

(A color version of this figure is available in the online journal.)

added in quadrature with $\sigma_{\bar{x}}$, to provide a total uncertainty in [*X*/H]. These total uncertainties are tabulated in Table 6 for all standard and program stars. While this yields an uncertainty for our abundance ratios in [*X*/H], we are interested in how elemental abundances vary with respect to iron. We calculated these uncertainties following Johnson (2002):

$$\sigma^2\,(\mathrm{A/B}) = \sigma^2\,(\mathrm{A}) + \sigma^2\,(\mathrm{B}) - 2\sigma_{\mathrm{A,B}}, \quad (1)$$

where the covariance between elements A and B ($\sigma_{A,B}$) is given by

$$\sigma_{A,B} = \left(\frac{\partial \log \epsilon_A}{\partial T_{\rm eff}}\right)\left(\frac{\partial \log \epsilon_B}{\partial T_{\rm eff}}\right)\sigma^2_{T_{\rm eff}} + \left(\frac{\partial \log \epsilon_A}{\partial \log g}\right)\left(\frac{\partial \log \epsilon_B}{\partial \log g}\right)\sigma^2_{\log g} + \left(\frac{\partial \log \epsilon_A}{\partial \xi}\right)\left(\frac{\partial \log \epsilon_B}{\partial \xi}\right)\sigma^2_{\xi} + \left[\left(\frac{\partial \log \epsilon_A}{\partial T_{\rm eff}}\right)\left(\frac{\partial \log \epsilon_B}{\partial \log g}\right) + \left(\frac{\partial \log \epsilon_A}{\partial \log g}\right)\left(\frac{\partial \log \epsilon_B}{\partial T_{\rm eff}}\right)\right]\sigma_{T_{\rm eff},\log g} + \left[\left(\frac{\partial \log \epsilon_A}{\partial \xi}\right)\left(\frac{\partial \log \epsilon_B}{\partial \log g}\right) + \left(\frac{\partial \log \epsilon_A}{\partial \log g}\right)\left(\frac{\partial \log \epsilon_B}{\partial \xi}\right)\right]\sigma_{\xi,\log g}. \quad (2)$$

The covariance between effective temperature and surface gravity was calculated by sampling the effective temperature and performing an ionization balance for the adjusted temperature. The resultant covariance is given as

$$\sigma_{T_{\rm eff},\log g} = \frac{1}{N}\sum_{i=1}^{N}\left(T_{{\rm eff},i} - \overline{T_{\rm eff}}\right)\left(\log g_i - \overline{\log g}\right). \quad (3)$$

Covariance between ξ and $\log g$ is calculated in the same manner. The total abundance uncertainty with respect to H and Fe (e.g., $\sigma([X/{\rm H}])$, $\sigma([X/{\rm Fe}])$) for all species is given in Table 6. These total uncertainties have been adopted in all figures throughout this text. Due to the cancellation of systematic effects, some abundance ratios with respect to iron have lower uncertainties than their quoted absolute abundance uncertainties.

4. DISCUSSION

4.1. Stream Membership

Given the low surface brightness of the Orphan stream, separating true members from interlopers can be particularly challenging. Before inferring any properties of the undiscovered parent satellite from our sample, we must examine whether our targets are truly stars from the disruption of the Orphan stream progenitor.

When compared against the mean of our high priority targets, the velocities of the low and medium probability candidates are +6.2 and −23.7 km s^{-1} different, respectively. Given that this region of the stream has a low intrinsic velocity dispersion (Casey et al. 2013a), the significantly lower velocity of the medium-probability target, OSS 18, is intriguing. Perhaps more concerning is that the low and medium probability candidates are markedly more metal-rich than the high-priority targets: [Fe/H] = −0.86 and −0.62 dex for OSS 3 and OSS 18, a difference of +0.45 and +0.28 dex from the low-resolution measurements, respectively. Spectroscopic studies suggest that the stream is significantly more metal-poor than [Fe/H] ∼ −0.8 dex (Belokurov et al. 2007; Newberg et al. 2010; Casey et al. 2013a; Sesar et al. 2013), making the association between the Orphan stream and OSS 3 or OSS 18 tenuous. It is also worth noting that these targets are the farthest candidates ($|B_{\rm Orphan}| \sim 0\overset{\circ}{.}5$) from the best-fit Orphan stream orbital plane deduced by Newberg et al. (2010). On the basis of the observables, we deduce that the lower probability members, OSS 3 and OSS 18, are unlikely to be disrupted Orphan stream members.

The three high-probability targets (OSS 6, 8, and 14) have velocities within 2.4 km s^{-1} of each other, consistent with the Orphan stream velocity. The velocities from high-resolution spectra confirm the very low line-of-sight velocity dispersion in this part of the stream. The metallicities of these targets are also in reasonable agreement with those found from low-resolution spectroscopy, implying that the candidates are ∼20 kpc away—at approximately the same distance as the Orphan stream. For the remainder of this discussion, we consider OSS 6, 8, and 14 to be true disrupted members of the Orphan stream.

4.2. Metallicity Distribution Function

Although the sample size is small, the three Orphan stream members have a wide range in metallicity, ranging from [Fe/H] = −1.58 to metal-poor [Fe/H] = −2.66. Not much can be said about the metallicity distribution, other than to say it is wide and inconsistent with a mono-metallic population (e.g., a globular cluster). Newberg et al. (2010) and Sesar et al. (2013) found the stream to have a mean metallicity of [Fe/H] = −2.1 from BHB and RR Lyrae stars. According to the metallicity gradient along the stream that was reported by Sesar et al. (2013), we might expect a higher mean metallicity than [Fe/H] > −2.1 in our sample closer to the celestial equator. We note that our metallicity spread of [Fe/H] = −1.58 to −2.66 is consistent with that of Sesar et al. (2013): [Fe/H] = −1.5 to −2.7, and the somewhat wider spread found by Newberg et al. (2010): [Fe/H] = −1.3 to −3.

A total metallicity spread as wide as ∼1 dex, or a standard deviation of $\sigma([{\rm Fe/H}]) = 0.56$ (Casey et al. 2013a), is consistent with the stochastic chemical enrichment of the present-day dSph galaxies (Mateo 1998; Kirby et al. 2011). This is also compatible with the constraints from the dynamical constraints inferred by the arc and width of the stream, which suggest that the progenitor is a dark matter-dominated system.

4.2.1. [α/Fe] Abundance Ratios

The abundance trends of individual elements track the star formation history of a cluster or galaxy. In the Milky Way, this is most evident by the evolution of α-element abundances with increasing metallicity. The α-elements were produced in massive stars before being ejected to the interstellar medium by Type II supernovae. Later, Type Ia supernovae began to contribute to the Galaxy's chemical enrichment by expelling iron (like Type II), but it did not produce significant amounts of α-elements. As such, a net decrease in [α/Fe] is observed upon the onset of Type Ia supernovae. This inflexion occurs in the Milky Way near [Fe/H] ∼ −0.7, decreasing toward Solar-like values.

Tolstoy et al. (2003) first noted that stars in the present-day dSph galaxies were separated in [α/Fe] from the majority of the Milky Way stars. In the dSph galaxies, a significant contribution of Type Ia supernovae was observable in [α/Fe] abundance ratios near [Fe/H] > −1.7 dex, with the exception of Draco, which shows low [α/Fe] at all metallicities. Some dSph stars also have a large range in [α/Fe] values, increasing up to that seen in field stars.

The Orphan stream stars have low [α/Fe] abundance ratios (∼0.22) with respect to the Milky Way sample (∼0.40 dex). The low- and medium-probability members—which we deem to be field interlopers—also have low [α/Fe] abundance ratios, but given their overall metallicity these α-element ratios are consistent with the thick disk enrichment of the Milky Way. Because our Orphan stream members (i.e., the high-probability members OSS 6, 8, and 14) are metal-poor, we can be confident

that we are not confusing their low-α signature for the standard chemical enrichment of the Milky Way.

We stress that [α/Fe], on its own, should never be used as a litmus test for accretion on to the Milky Way. One must carefully select candidates that appear to be stream members based on all the observables, and then examine their detailed abundances in order to infer the chemical evolution of the disrupted host. We are already quite confident that these stars are truly disrupted Orphan stream members, and as such, we can say that the low [α/Fe] abundance ratios observed in the Orphan stream are consistent with the low α-element enhancement of the present-day dSph galaxies.

4.2.2. [Ba/Y]

Differences in [Ba/Y] ratios between the present-day dSph stars and the Milky Way have been observed by several groups (Shetrone et al. 2003; Venn et al. 2004). A number of possible explanations have been proposed to explain this offset, including changes in SNe II yields—or by changing the frequency of SNe II explosions via adjustments to the initial mass function—or altering the influence of α-rich freeze-out (e.g., see Venn et al. 2004 for a discussion).

Arbitrarily adjusting SNe II yields between two different nucleosynthesis sites appears a somewhat unlikely scenario. By employing SN frequency corrections in addition to using adjusted yields, Qian & Wasserburg (2001) can reproduce the low [Ba/Y] trends in the Galaxy, but not the high [Ba/Y] ratios observed in the dSph galaxies. Alternatively, leaving SNe II yields unchanged, these offsets could be reproduced by simply adjusting the frequency of SNe II events through the truncation of the upper initial mass function (IMF). In effect, massive stars would be less numerous, because they are thought to be the primary production sites for the first n-capture peak elements (e.g., yttrium in this case). Because higher α-element yields are also expected for massive stars, this may affect both the [Ba/Y] abundance and the overall [α/Fe] abundance. However, whether the upper IMF differs between the dSph and the Milky Way remains an open question.

We have lower limits in [Ba/Y] for all the Orphan stream stars. This is because Y was not detected in any of the stream stars. The standard stars and lower probability stream targets all have [Ba/Y] ratios that are consistent with the Milky Way for their given overall metallicity, as shown in Figure 2. Although we only have lower limits for [Ba/Y], in OSS 6 and OSS 8 these are $\sim$+0.5 dex offset from the main component of the Milky Way. This is a similar offset from that observed in the present-day dSphs, as compiled by Venn et al. (2004). For the most metal-poor stream star, OSS 14, our limit on Y abundance yields a weak—but consistent—lower limit of [Ba/Y] > -0.97 dex. We note that robust lower limits for [Ba/Y] in the most metal-poor dSph stars ([Fe/H]< -2) are difficult to ascertain.

4.3. Possible Parent Systems

A number of associations have been proposed between the Orphan stream and known Milky Way satellites. However, most have been shown to be either unlikely or implausible. Here we discuss the possibility of association between the Orphan stream and NGC 2419, as well as Segue 1.

4.3.1. NGC 2419

The width and length of a tidal tail are a clear indication of the nature of the parent satellite. For the case of the Orphan stream, these characteristics favor a dark-matter-dominated system (e.g., a dwarf galaxy). However, given the large apogalacticon of 90 kpc for the Orphan stream, a relationship has been proposed between the Orphan stream and NGC 2419 (Brüns & Kroupa 2011). NGC 2419 is the most distant ($D \sim 85$ kpc)—and most luminous ($M_V \sim -9.6$)—globular cluster in the Milky Way halo ($D > 20$ kpc). Just like the Orphan stream, the system is also quite metal-poor: [Fe/H] = –2.15.

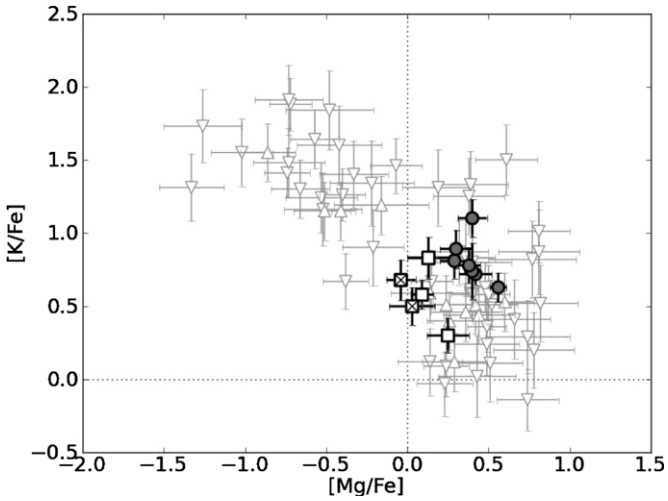

Figure 3. Magnesium and potassium abundance ratios for stars in the globular cluster NGC 2419 from Cohen et al. (2011; △) and Mucciarelli et al. (2012; ▽). Standard stars and Orphan stream candidates are shown with the same markers used in Figure 1.

Stars in globular clusters are known to exhibit peculiar chemical patterns, most notably in an anti-correlation between sodium and oxygen abundances (e.g., Carretta et al. 2009). Following this, NGC 2419 is particularly special because it shows an unusual anti-correlation between magnesium and potassium, which is even stronger than the classical Na–O anti-correlation. So far this chemical signature is unique to NGC 2419, and illustrates the most extreme cases of Mg-depletion and K-enhancement seen anywhere in the Milky Way, or its satellite systems (Cohen et al. 2011; Mucciarelli et al. 2012).

We do not find any that Orphan stream stars were extremely depleted in [Mg/Fe] or enhanced in [K/Fe] (Figure 3), as found in NGC 2419 (Cohen et al. 2010, 2011; Mucciarelli et al. 2012). If we consider two sub-populations in NGC 2419—a Mg-poor, K-rich and a Mg-normal, K-poor sample—then a two sample Kolmogorov–Smirnoff test demonstrates that we can be at least 99.7% confident that our Orphan stream members are inconsistent with being drawn from the Mg-poor NGC 2419 population. We cannot make such statements about the Mg-normal population, because abundances for that sample are typical for the Milky Way. The Mg-poor and Mg-normal sub-populations each comprise about half of the observed NGC 2419 population (Mucciarelli et al. 2012). Given the uniqueness of the Mg–K anti-correlation, a single Orphan stream star with significant Mg-depletion or K-enhancement would have provided an exciting hint for the Orphan stream parent. However, given the stream's large metallicity spread (Casey et al. 2013a; Sesar et al. 2013), this indicates the stream is unlikely to be associated with NGC 2419 given the cluster's small dispersion in overall metallicity (0.17 dex; Mucciarelli et al. 2012). We therefore firmly rule out any association between NGC 2419 and the Orphan stream.

4.3.2. Segue 1

The only known satellite system with an ambiguous association with the Orphan stream is Segue 1. The system resides in a particularly crowded region of the sky—it lies extremely close to the perigalacticon of the Orphan stream, and just south of the bifurcated Sagittarius stream. The original discovery of Segue 1 by Belokurov et al. (2007) suggested the system was an extended globular cluster, until recent studies showed that the system was an ultrafaint dwarf galaxy (Geha et al. 2009; Norris et al. 2010; Simon et al. 2011). The similarities between Segue 1 and the Orphan stream are striking. In addition to being nearby on the sky, Segue 1's distance of 23 kpc is consistent with the closest portion of the Orphan stream. The velocities between the two systems are also coincident: +114 km s^{-1} for Segue 1 and ∼+120 km s^{-1} for the nearest portion of the stream. Additionally, both systems exhibit extremely low velocity dispersions, on the order of 3–8 km s^{-1}. However, stars linking the two systems have yet to be found. The association between the two is not obvious. As Gilmore et al. (2013) summarizes, "*are they just ships passing in the dark night?*"

The characteristics of the Orphan stream are clues to the nature of its progenitor: the arc length and intrinsic width suggests the parent system must be dark-matter-dominated. Segue 1 is the most dark-matter-dominated system known, such that it has become a prime focus for indirect dark matter detection experiments (Essig et al. 2010; Baushev et al. 2012). However, there are some doubts as to whether Segue 1 has experienced any tidal effects (Niederste-Ostholt et al. 2009; Simon et al. 2011). Segue 1 is well within the galactic tidal field, and initial indications of east–west tidal effects (Niederste-Ostholt et al. 2009) seem to have been complicated by the crowded region bordering the system (Simon et al. 2011). Presently, no stars or tails clearly connecting the two systems have been found.

The chemistry of Segue 1 is particularly relevant here. Segue 1 hosts an extremely wide range of stellar metallicities: the mean is found to be [Fe/H] = −2.5 and the spread extends from [Fe/H] = −3.4 to −1.6 dex (Simon et al. 2011). There is significant overlap between the metallicity distributions reported for Segue 1 and the Orphan stream. The high-resolution spectra in this study confirm the wide metallicity range of the Orphan stream members found by Casey et al. (2013a), and independently reported by Sesar et al. (2013) ([Fe/H] = −1.5 to −2.7). Thus, in addition to on-sky position, distances, velocity, and velocity dispersion, Segue 1 and the Orphan stream share a wide and consistent range in metallicities. In contrast to these observables, Vargas et al. (2013) and Frebel et al. (submitted) find Segue 1 members to be extremely α-enhanced ([α/Fe] > 0.4), unlike what we observed in the disrupted Orphan stream members.

We note that although the two systems appear to be related in some respect, if Segue 1 were the "parent" of the Orphan stream the differing [α/Fe] abundances and lack of tidal features surrounding Segue 1—after extensive examination—is somewhat puzzling. Furthermore if Segue 1 is the disrupted host, and if the stream metallicity gradient presented by Sesar et al. (2013) is correct, it implies that the stream becomes more metal-rich at greater distances from the parent system, contrary to what is typically observed.

5. CONCLUSIONS

We present a chemical analysis of five Orphan stream candidates, three of which we confirm are true members from the disrupted Orphan stream parent satellite. The two non-members were both originally identified to have "low" or "medium" probability of stream membership from the low-resolution spectroscopy by Casey et al. (2013a). We encourage high-resolution spectroscopic follow-up of the remaining high-probability Orphan stream members presented in Casey et al. (2013a).

This work demonstrates the first detailed chemical study of the Orphan stream from high-resolution spectra. A large metallicity spread is present in the Orphan stream members, confirming the work by Casey et al. (2013a) and Sesar et al. (2013) that the Orphan stream is not mono-metallic. The spread in overall metallicity is consistent with the internal chemical evolution of the present-day dwarf galaxies. Detailed chemical abundances confirm this scenario. Low [α/Fe] element ratios were observed in the stream stars, and lower limits of [Ba/Y] were ascertained, which sit well above the bulk component of the Milky Way for two of the three stream members. Thus, we present the first detailed chemical evidence that the parent of the Orphan stream is a dwarf galaxy.

On the basis of chemistry, we exclude the extended globular cluster NGC 2419 as a plausible parent to the Orphan stream. No firm link between Segue 1 and the Orphan stream has been identified. While the wide range in metallicities adds to the phase-space similarities between the two systems, the substantial difference in [α/Fe] abundance ratios places doubt on any association. It appears that the disrupting dwarf galaxy parent may reside in the southern sky, just waiting to be discovered.

A.R.C. is grateful to Martin Asplund, David Yong, Amanda Karakas, Ana Bonaca, and Josh Simon for fruitful discussions and commentary on this work. Australian access to the Magellan Telescopes was supported through the National Collaborative Research Infrastructure Strategy of the Australian Federal Government. A.R.C. acknowledges the financial support through the Australian Research Council Laureate Fellowship LF0992131. S.C.K. and G.D.C. acknowledge the financial support from the Australian Research Council through Discovery Program DP120101237. A.F. acknowledges support from NSF grant AST-1255160.

REFERENCES

Allende Prieto, C., Lambert, D. L., & Asplund, M. 2001, ApJ, 556, 63
Asplund, M., Grevesse, N., Sauval, A. J., & Scott, P. 2009, ARA&A, 47, 481
Baushev, A. N., Federici, S., & Pohl, M. 2012, PhRvD, 86, 063521
Bell, E. F., Zucker, D. B., Belokurov, V., et al. 2008, ApJ, 680, 295
Belokurov, V., Evans, N. W., Irwin, M. J., et al. 2007, ApJ, 658, 337
Belokurov, V., Zucker, D. B., Evans, N. W., et al. 2006, ApJ, 642, 137
Bernstein, R., Shectman, S. A., Gunnels, S. M., Mochnacki, S., & Athey, A. E. 2003, Proc. SPIE, 4841, 1694
Brüns, R. C., & Kroupa, P. 2011, ApJ, 729, 69
Carretta, E., Bragaglia, A., Gratton, R. G., et al. 2009, A&A, 505, 117
Casey, A. R., Da Costa, G., Keller, S. C., & Maunder, E. 2013a, ApJ, 764, 39
Casey, A. R., Keller, S. C., Frebel, A., et al. 2013b, MNRAS, submitted (arXiv:1309.3562)
Castelli, F., & Kurucz, R. L. 2004, arXiv:astro-ph/0405087
Cohen, J. G., Huang, W., & Kirby, E. N. 2011, ApJ, 740, 60
Cohen, J. G., Kirby, E. N., Simon, J. D., & Geha, M. 2010, ApJ, 725, 288
Deason, A. J., Belokurov, V., Evans, N. W., et al. 2012, MNRAS, 425, 2840
De Silva, G. M., Freeman, K. C., Bland-Hawthorn, J., Asplund, M., & Bessell, M. S. 2007, AJ, 133, 694
Drake, A. J., Catelan, M., Djorgovski, S. G., et al. 2013, ApJ, 765, 154
Eggen, O. J., Lynden-Bell, D., & Sandage, A. R. 1962, ApJ, 136, 748
Essig, R., Sehgal, N., Strigari, L. E., Geha, M., & Simon, J. D. 2010, PhRvD, 82, 123503
Fellhauer, M., Evans, N. W., Belokurov, V., et al. 2007, MNRAS, 375, 1171
Frebel, A., Casey, A. R., Jacobson, H. R., & Yu, Q. 2013, ApJ, 769, 57

Frebel, A., Simon, J. D., Geha, M., & Willman, B. 2010, ApJ, 708, 560
Freeman, K., & Bland-Hawthorn, J. 2002, ARA&A, 40, 487
Fulbright, J. P. 2000, AJ, 120, 1841
Geha, M., Willman, B., Simon, J. D., et al. 2009, ApJ, 692, 1464
Gilmore, G., Koposov, S., Norris, J. E., et al. 2013, Msngr, 151, 25
Gratton, R. G., & Sneden, C. 1991, A&A, 241, 501
Gratton, R. G., Sneden, C., Carretta, E., & Bragaglia, A. 2000, A&A, 354, 169
Grillmair, C. J. 2006, ApJ, 645, 37
Grillmair, C. J., & Dionatos, O. 2006a, ApJ, 641, 37
Grillmair, C. J., & Dionatos, O. 2006b, ApJ, 643, 17
Grillmair, C. J., & Johnson, R. 2006, ApJ, 639, 17
Hambly, N. C., MacGillivray, H. T., Read, M. A., et al. 2001, MNRAS, 326, 1279
Harris, W. E. 1996, AJ, 112, 1487
Helmi, A. 2008, A&ARv, 15, 145
Ibata, R. A., Gilmore, G., & Irwin, M. J. 1994, Natur, 370, 194
Ishigaki, M. N., Aoki, W., & Chiba, M. 2013, ApJ, 771, 67
Jin, S., & Lynden-Bell, D. 2007, MNRAS, 378, 64
Johnson, J. A. 2002, ApJS, 139, 219
Johnston, K. V. 1998, ApJ, 495, 297
Kirby, E. N., Lanfranchi, G. A., Simon, J. D., Cohen, J. G., & Guhathakurta, P. 2011, ApJ, 727, 78
Koposov, S., de Jong, J. T. A., Belokurov, V., et al. 2007, ApJ, 669, 337
Majewski, S. R., Nidever, D. L., Smith, V. V., et al. 2012, ApJ, 747, 37
Mateo, M. L. 1998, ARA&A, 36, 435
Morrison, H. L. 1993, AJ, 106, 578
Mucciarelli, A., Bellazzini, M., Ibata, R., et al. 2012, MNRAS, 426, 2889
Newberg, H. J., Willett, B. A., Yanny, B., & Xu, Y. 2010, ApJ, 711, 32
Niederste-Ostholt, M., Belokurov, V., Evans, N. W., et al. 2009, MNRAS, 398, 1771
Nissen, P. E., Chen, Y. Q., Schuster, W. J., & Zhao, G. 2000, A&A, 353, 722
Norris, J. E., Wyse, R. F. G., Gilmore, G., et al. 2010, ApJ, 723, 1632
Odenkirchen, M., Grebel, E. K., Dehnen, W., et al. 2003, AJ, 126, 2385
Price-Whelan, A. M., & Johnston, K. V. 2013, ApJL, 778, L12
Qian, Y.-Z., & Wasserburg, G. J. 2001, ApJ, 559, 925
Racine, R., & Harris, W. E. 1975, ApJ, 196, 413
Roederer, I. U., Sneden, C., Thompson, I. B., Preston, G. W., & Shectman, S. A. 2010, ApJ, 711, 573
Sales, L. V., Helmi, A., Starkenburg, E., et al. 2008, MNRAS, 389, 1391
Searle, L., & Zinn, R. 1978, ApJ, 225, 357
Sesar, B., Grillmair, C. J., Cohen, J. G., et al. 2013, ApJ, 776, 26
Shetrone, M., Venn, K. A., Tolstoy, E., et al. 2003, AJ, 125, 684
Shetrone, M. D. 1996, AJ, 112, 1517
Simon, J. D., Geha, M., Minor, Q. E., et al. 2011, ApJ, 733, 46
Starkenburg, E., Helmi, A., Morrison, H. L., et al. 2009, ApJ, 698, 567
Tolstoy, E., Hill, V., & Tosi, M. 2009, ARA&A, 47, 371
Tolstoy, E., Venn, K. A., Shetrone, M., et al. 2003, AJ, 125, 707
Tonry, J., & Davis, M. 1979, AJ, 84, 1511
Vargas, L. C., Geha, M., Kirby, E. N., & Simon, J. D. 2013, ApJ, 767, 134
Venn, K. A., Irwin, M., Shetrone, M. D., et al. 2004, AJ, 128, 1177
Venn, K. A., Irwin, M., Shetrone, M. D., et al. 2006, AJ, 132, 1726
Woosley, S. E., & Weaver, T. A. 1995, ApJS, 101, 181
Wylie-de Boer, E., Freeman, K., & Williams, M. 2010, AJ, 139, 636
Xue, X. X., Rix, H. W., Zhao, G., et al. 2008, ApJ, 684, 1143
Yong, D., Carney, B. W., & Teixera de Almeida, M. L. 2005, AJ, 130, 597
Yong, D., Norris, J. E., Bessell, M. S., et al. 2013, ApJ, 762, 26